SANDIA REPORT

SAND2003-4314
Unlimited Release
Printed December 2003

Anomalies in the Theory of Viscous Energy Losses due to Shear in Rotational MEMS Resonators

Jeffrey L. Dohner, Mark Jenkins, Timothy Walsh, Kelly Klody

Prepared by
Sandia National Laboratories
Albuquerque, New Mexico 87185 and Livermore, California 94550

Sandia is a multiprogram laboratory operated by Sandia Corporation,
a Lockheed Martin Company, for the United States Department of Energy's
National Nuclear Security Administration under Contract DE-AC04-94AL85000.

Sandia National Laboratories

Issued by Sandia National Laboratories, operated for the United States Department of Energy by Sandia Corporation.

Printed in the United States of America. This report has been reproduced directly from the best available copy.

Available to DOE and DOE contractors from
U.S. Department of Energy
Office of Scientific and Technical Information
P.O. Box 62
Oak Ridge, TN 37831

Telephone: (865)576-8401
Facsimile: (865)576-5728
E-Mail: reports@adonis.osti.gov
Online ordering: http://www.doe.gov/bridge

Available to the public from
U.S. Department of Commerce
National Technical Information Service
5285 Port Royal Rd
Springfield, VA 22161

Telephone: (800)553-6847
Facsimile: (703)605-6900
E-Mail: orders@ntis.fedworld.gov
Online order: http://www.ntis.gov/help/ordermethods.asp?loc=7-4-0#online

SAND2003-4314
Unlimited Release
Printed December 2003

Anomalies in the Theory of Viscous Energy Losses due to Shear in Rotational MEMS Resonators

Jeffrey L. Dohner, Mark Jenkins
MEMS Device Technologies

Timothy Walsh
Computational Solid Mechanics & Structural Dynamics

Kelly Klody
Electromechanical Engineering

Sandia National Laboratories
P.O. Box 5800
Albuquerque, NM 87185

Abstract

In this paper, the effect of viscous wave motion on a micro rotational resonator is discussed. This work shows the inadaquacy of developing theory to represent energy losses due to shear motion in air. Existing theory predicts Newtonian losses with little slip at the interface. Nevertheless, experiments showed less effect due to Newtonian losses and elevated levels of slip for small gaps. Values of damping were much less than expected. Novel closed form solutions for the response of components are presented. The stiffness of the resonator is derived using Castigliano's theorem, and viscous fluid motion above and below the resonator is derived using a wave approach. Analytical results are compared with experimental results to determine the utility of existing theory. It was found that existing macro *and* molecular theory is inadequate to describes measured responses.

Intentionally Left Blank

Acknowledgements

The authors would like to thank David Sandison and Jim Redmond for their financial support. They would also like to thank John Torczynki for his technical feedback in the area of molecular modeling and Harold Statfford for his feedback in the area of micro systems and acoustics.

Intentionally Left Blank

Table of Contents:

Energy Damping Due to Viscous Wave Propagation in a Micro-scale Rotational Resonator

List of Figures:

List of Figures continued:

Introduction

In many micromechanical devices, a significant amount of energy is lost due to fluid damping. This can hinder the performance of the device by requiring larger amounts of power, reduced sensitivity, slow structural response, or reduced Q. These losses are often classified into two categories -

- squeeze-film damping and
- damping due to lateral oscillations.

Squeeze-film damping occurs when a fluid is pressed between two surfaces. This pressing produces fluid motion that gives rise to viscous flow and energy loss. This category of energy loss has been well studied using both numerical and closed form analysis, and therefore, will not be discussed here.

Damping due to lateral oscillations occurs due to the shearing of fluid and is far less studied. Y. Cho et al. [1,2] showed that a viscous wave approach can be used to describe this type of energy loss. They produced enhanced predictions of damping in a vibrating comb drive by coupling the motion of the drive to a viscous wave solution. Wenzel [3] also used this type of approach to account for energy losses in a flexural plate wave sensor operating below coincidence. Neglecting edge effects, Wenzel solved for the coupling between the plate and fluid in closed form. Dohner [4] expanded upon Wenzel's analytical work by including edge effects. He was able to show that a fluid/structure resonance occurs near to coincidence. This resonance can draw enough energy from the plate as to render a sensor nonfunctional. Nevertheless, Dohner did not include the effect of slip conditions.

In the following, a wave approach will be used to determine energy losses from a vibrating disk. Theory will be derived and experiments performed to determine if the damped response of the disk can be predicted using existing theory. It will be shown that this theory is inadequate to describe the response of the disk as the gap between the disk and the substrate is reduced.

Theory

To understand the effects of viscous wave propagation on surface micro-machined devices, test structures were manufactured using SUMMiT V^{TM} technology [5]. Figure 1 illustrates one of these devices [6]. This device consist of an annular disk of inner radius r_i and outer radius r_o. The disk is of thickness t and is a distance g above the substrate. The interior of the disk is connected to a torsional spring with a hub radius of r_h and a thickness, w. The disk and spring are constructed from the same material, polysilicon with Young's Modulus E and density ρ. The center line of the spring, $r_c(\theta)$, is defined by the equation

$$r_c(\theta) = a - b\theta \tag{1a}$$

where

$$a = \frac{r_i - r_h}{\theta_h - \theta_i}\theta_h + r_h \tag{1b}$$

$$b = \frac{r_i - r_h}{\theta_h - \theta_i} \tag{1c}$$

$r_c(\theta_i) = r_i$ and $r_c(\theta_h) = r_h$. The structure is submerged in air with density ρ_o and with shear viscosity μ_o. Locations on the disk and in the ambient fluid are

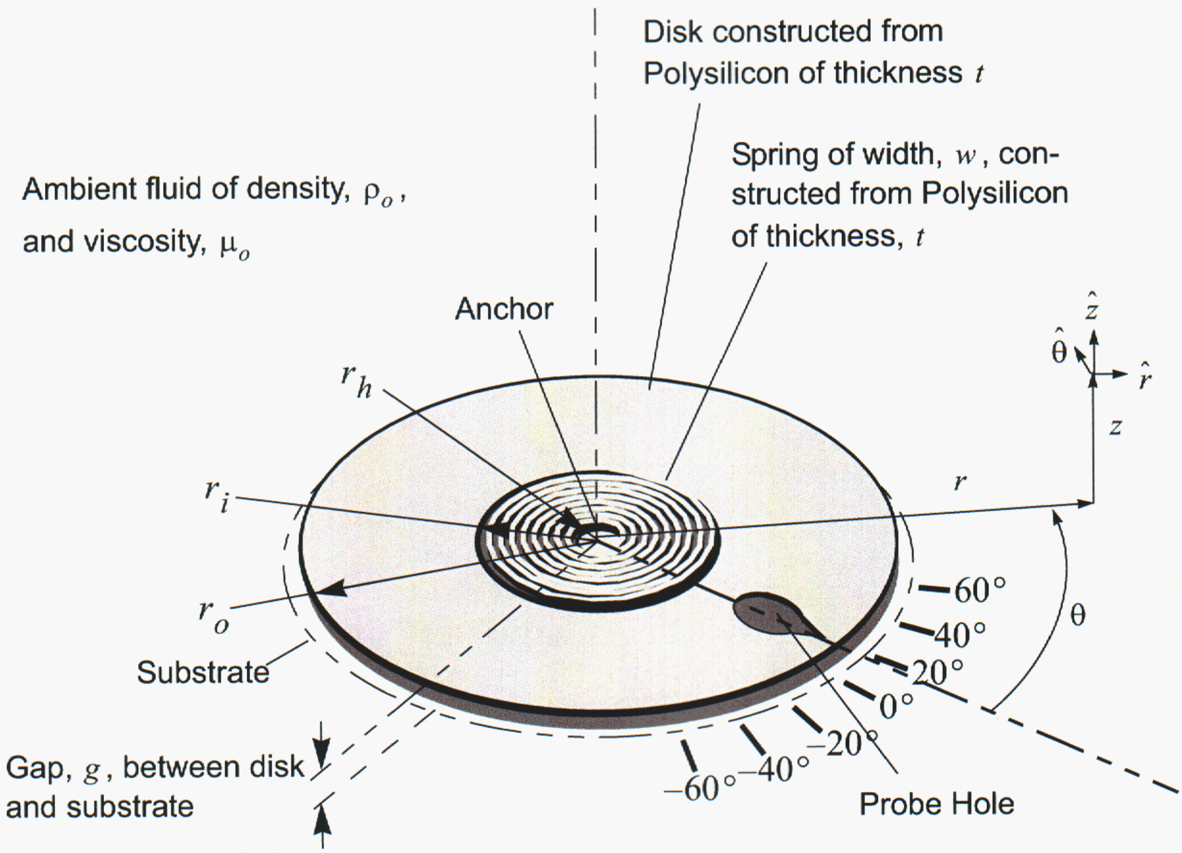

Figure 1: Micro Disk Attached to a Torsional Spring

defined by using the cylindrical coordinate system (r, θ, z) where $(r, \theta, z) = (0, 0, 0)$ is located at the center of the upper surface of the disk and $\hat{r}, \hat{\theta}, \hat{z}$, are unit vectors. Numerical values for the parameters presented above are given in Table 1 in the Appendix. Two micro disk were considered - one with a gap of $10.5\mu m$ and the other with a gap of $2.0\mu m$.

The Figure 1 device was modeled by analyzing the forces on the disk due to the stiffness, inertia, and viscosity. The spring was modeled using Castigliano's theorem; inertia was modeled using the conservation of momentum; and viscous forces on the top and bottom of the disk were modeled using wave theory. Component models were then combined to construct the equation of motion for the device.

Spring Stiffness

Figure 2 is an illustration of the center line of the spring, $r_c(\theta)$. Using Castigliano's theorem [7], a closed from solution for the stiffness of the spring was determined. This theorem states that if F_s is a force applied to the end of the spring and u_s is a collocated displacement, then

$$u_s = \frac{\partial U}{\partial F_s} \qquad (2)$$

where U is the total energy within the spring.

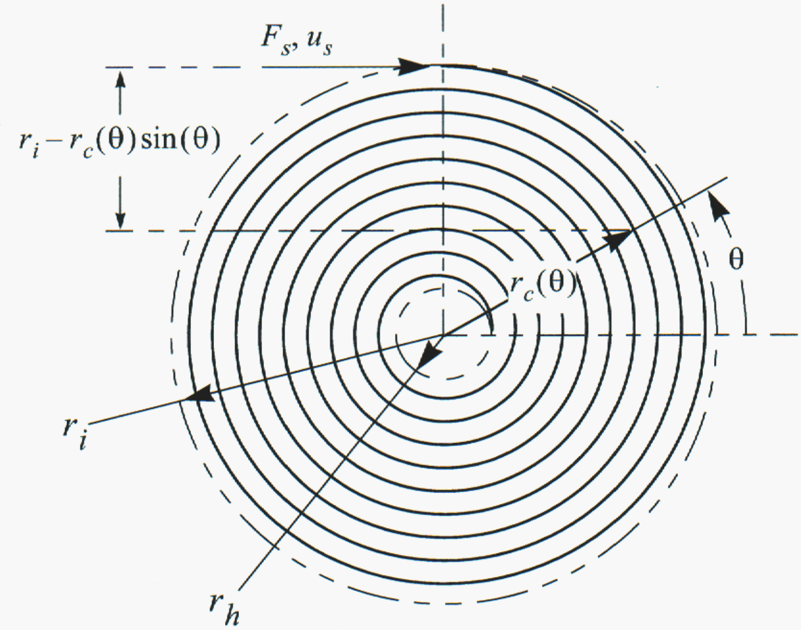

Figure 2: Trajectory of Center Line of Torsional Spring

Assuming that the majority of the energy within the spring is stored in bending,

$$U = \int_{\theta_i}^{\theta_h} \frac{M^2}{2EI} r_c(\theta)\, d\theta \qquad (3)$$

where M is the moment at any $r_c(\theta)$, and $I = tw^3/12$.

Assuming that $\theta_h = 2\pi \cdot n + \pi/2 + \theta_i$,

$$M(r(\theta)) = F_s(r_i - r_c(\theta)\sin(\theta)) \quad . \qquad (4)$$

Substituting (4) into (3) gives,

$$U = \frac{F_s^2}{2EI} \int_{\theta_i}^{\theta_h} (r_i - r_c(\theta)\sin(\theta))^2 r_c(\theta)\, d\theta \qquad (5a)$$

and substituting (1) into (5a), expanding and integrating gives

$$\frac{u_s}{F_s} = \frac{1}{K} = \frac{1}{EI}\left\{ a r_i^2 \theta - b r_i^2 \frac{\theta^2}{2} \right.$$

$$+ 2a^2 r_i \cos\theta + 4abr_i(\sin\theta - \theta\cos\theta)$$

$$-2b^2 r_i(2\theta\sin\theta - (\theta^2 - 2)\cos\theta)$$

$$+ a^3\left(\frac{\theta}{2} - \frac{1}{4}\sin 2\theta\right)$$

$$-3a^2 b\left(\frac{\theta^2}{4} - \frac{\theta}{4}\sin 2\theta - \frac{\cos 2\theta}{8}\right)$$

$$+3ab^2\left(\frac{\theta^3}{6} - \left(\frac{\theta^2}{4} - \frac{1}{8}\right)\sin 2\theta - \frac{\theta}{4}\sin 2\theta\right)$$

$$\left. -b^3\left(\frac{\theta^4}{8} - \left(\frac{\theta^3}{4} - \frac{3\theta}{8}\right)\sin 2\theta\right)\right\}\Bigg|_{\theta_i}^{\theta_h} \qquad (5b)$$

where K is the collocated linear stiffness of the spring. If T_s is the torque that spring exerts on the disk, then

$$\mathsf{K} = \frac{T_s}{\theta} = K r_i^2 \qquad (5c)$$

where K is the torsional stiffness of the spring.

Inertia

Using standard methods, the torque on the disk, T_d, due to inertial effects can be found as

$$M = \frac{T_d}{\ddot{\theta}} = \frac{\pi \rho t}{2}(r_o^4 - r_i^4)\,. \qquad (6)$$

Continuum Assumption and Boundary Conditions

In this paper, it is assumed that the fluid is air. Since the mean free path of air at standard conditions is $\lambda = 0.06 \mu m$ [8], 175 mean free paths exist between the disk and substrate of a device with $g = 10.5 \mu m$ and 33 mean free paths exist between the disk and substrate of a device with a gap of $2.0 \mu m$. Moreover, the shear velocity in air is $c_s = \sqrt{\frac{2\omega\mu_o}{\rho_o}}$. For $f = 1000 Hz$, there are 5123 mean free paths. Therefore, the assumption of air being a continuum is reasonable for frequencies at below $f = 1000 Hz$ and geometries discussed here.

Boundary conditions are dependent upon the Knudsen number, Kn, which is equal to the mean free path over a characteristic distance [8,9]. For flat parallel plates, the characteristic distance is g. For $g = 10.5 \mu m$, $Kn = 0.0057$ which is in the no slip region. For $g = 2.0 \mu m$, $Kn = 0.03$ which is in the slip range. Therefore, slip boundary conditions must be considered.

From existing theory, the effect of slip at the boundaries can be examined. Consider the case of two parallel plates - one fixed and the other traveling at a velocity of U_w (Figure 3). If $Kn = 0.03$ then, from existing theory, the slip condition must be considered but the fluid can still be treated as Newtonian. From molecular theory [9]

$$U_t + \zeta\frac{\partial U}{\partial z}\bigg|_{z=g} = U_w \qquad (7a)$$

$$U_b = \zeta\frac{\partial U}{\partial z}\bigg|_{z=0} \qquad (7b)$$

where

$$\zeta = \frac{2-\sigma_v}{\sigma_v}\lambda\,, \qquad (7c)$$

σ_v is the tangential momentum accommodation coefficient (a value between 0.2 and

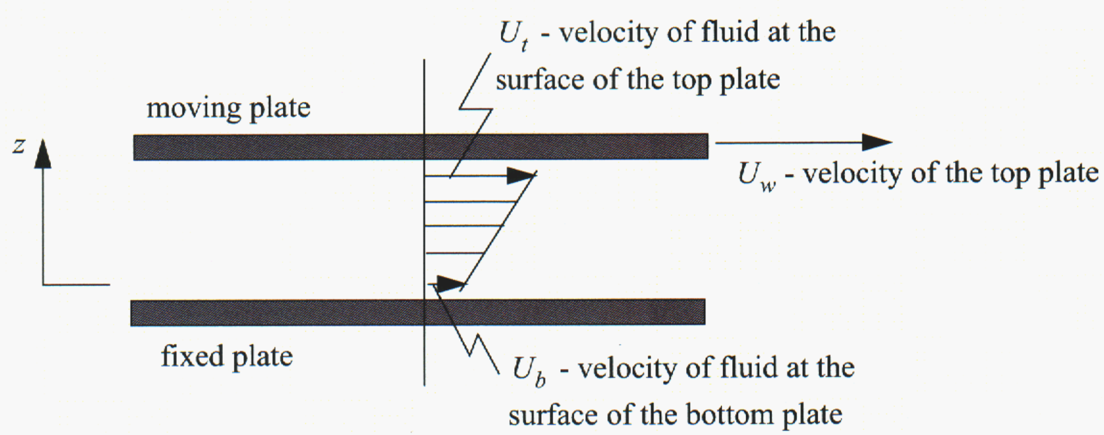

Figure 3: Parallel Plate configuration

0.8), U_t is the velocity of the fluid near to the moving plate and U_b is the velocity of the fluid near to the fixed plate. Assuming a linear velocity distribution through the gap, this gives

$$\begin{bmatrix} U_t \\ U_b \end{bmatrix} = \begin{bmatrix} \dfrac{1+\zeta/g}{1+2(\zeta/g)} \\ \dfrac{\zeta/g}{1+2(\zeta/g)} \end{bmatrix} U_w . \qquad (7d)$$

For example, for air with σ_v=0.8, g=2.0μm,

$$\begin{bmatrix} U_t \\ U_b \end{bmatrix} = \begin{bmatrix} 0.958 \\ 0.041 \end{bmatrix} U_w . \qquad (7e)$$

As can be seen from this example, existing theory states that the slip condition is important, but not dominant. For this example, the variation in boundary conditions with and without this condition is less than 5%. Nevertheless, as will be shown later, just the opposite is true. The slip condition dominates the response.

Fluid Loading on the Top of the Disk

The interaction of waves on top of the disk is complex. In this section, we will develop a closed form solution for fluid loading on the top of the disk using a wave approach.

For wave propagation in a viscous fluid, the velocity of the fluid can be represented by

$$\dot{\vec{u}} = \nabla\phi + \nabla \times \vec{\psi} \qquad (8a)$$

where ϕ is a scalar potential function, and $\vec{\psi}$ is a vector potential. Since $\vec{\psi}$ has no dilatational component, we applied the additional constraint,

$$\nabla \cdot \vec{\psi} = 0 . \qquad (8b)$$

Moreover, from Figure 1, only shear waves will result from the motion of the disk. These shear waves will have a displacement component only in the $\hat{\theta}$ direction. Therefore, $\phi = 0$, $\dot{\vec{u}} = u_\theta \hat{\theta}$, and $\vec{\psi} = \psi_r \hat{r} + \psi_z \hat{z}$. Thus, equations 8a and b become [10],

$$u_\theta = -\left(\frac{\partial \psi_z}{\partial r} - \frac{\partial \psi_r}{\partial z}\right) \text{ and } \qquad (9a)$$

$$\frac{1}{r}\frac{\partial}{\partial r}(r\psi_r) + \frac{\partial \psi_z}{\partial z} = 0 \qquad (9b)$$

In cylindrical coordinates, the equations of motion for a shear wave propagating in a viscous fluid [11,12] are given by

$$\frac{1}{\nu_o}\frac{\partial \psi_r}{\partial t} = \nabla^2 \psi_r - \frac{\psi_r}{r} \qquad (10a)$$

$$\frac{1}{\nu_o}\frac{\partial \psi_z}{\partial t} = \nabla^2 \psi_z \qquad (10b)$$

where

$$\nabla^2 = \frac{\partial^2}{\partial r^2} + \frac{1}{r}\frac{\partial}{\partial r} + \frac{\partial^2}{\partial z^2} \qquad (10c)$$

and $\nu_o = \mu_o / \rho_o$ is the kinematic viscosity of the fluid. From equation 7abc, the boundary conditions are given by

$$\left.\left(\dot{\vec{u}} - \zeta \frac{\partial}{\partial z}(\dot{\vec{u}} \cdot \hat{\theta})\right)\right|_{z=0} = \begin{cases} \dot{\theta} r \hat{\theta} & \text{for } r_i \le r \le r_o \\ 0 & \text{otherwise} \end{cases} \qquad (10d)$$

Equations 10a-d represent the equations of motion and boundary conditions required to describe wave motion above the disk. We will first transform these equation into the Laplace domain and then into the Hankel domain and then inverse transform them to obtain a closed form solution for the torque on the top of the disk.

For zero initial conditions, the Laplace transform of 10a and b is given by

$$0 = \nabla^2\varphi_r - \frac{\varphi_r}{r} - \frac{s}{\nu_o}\varphi_r \quad (11a)$$

$$0 = \nabla^2\varphi_z - \frac{s}{\nu_o}\varphi_z \quad (11b)$$

where $\varphi_r(s) = \int_0^\infty \psi_r(t)e^{-st}dt$ and

$\varphi_z(s) = \int_0^\infty \psi_z(t)e^{-st}dt$. The Laplace transform of 9b is given by

$$\frac{1}{r}\frac{\partial}{\partial r}(r\varphi_r) + \frac{\partial\varphi_z}{\partial z} = 0. \quad (11c)$$

Substituting 9a into 10d and taking the Laplace transform gives

$$\left(u_\theta - \zeta\frac{\partial u_\theta}{\partial z}\right)\bigg|_{z=0} = -\left(\frac{\partial\varphi_z}{\partial r} - \frac{\partial\varphi_r}{\partial z}\right)\bigg|_{z=0}$$

$$= \begin{cases} \dot{\theta}r & \text{for} \quad r_i \le r \le r_o \\ 0 & \text{otherwise} \end{cases} \quad (11d)$$

where $u_\theta = \int_0^\infty u_\theta(t)e^{-st}dt$.

Equations 11a-d represent the equations of motion and boundary conditions in the Laplace domain. Next, we will transform these equations into the Hankel domain.

Taking the Hankel transform [13,14] of order one of equations 11a and the Hankel transform of order zero of equation 11b gives

$$\left\{\frac{\partial^2}{\partial z^2} - \left(\gamma^2 + \frac{s}{\nu_o}\right)\right\}\tilde{\varphi}_r^1 = 0 \quad (12a)$$

$$\left\{\frac{\partial^2}{\partial z^2} - \left(\gamma^2 + \frac{s}{\nu_o}\right)\right\}\tilde{\varphi}_z^0 = 0 \quad (12b)$$

where $\mathcal{H}_1(\varphi_r) = \tilde{\varphi}_r^1 = \int_0^\infty \varphi_r J_1(\gamma r)rdr$,

$\mathcal{H}_0(\varphi_z) = \tilde{\varphi}_z^0 = \int_0^\infty \varphi_z J_0(\gamma r)rdr$. Taking the Hankel transform of order zero of equation 11c and noting that

$\mathcal{H}_0\left(\frac{1}{r}\frac{\partial}{\partial r}(r\varphi_r)\right) = \gamma\tilde{\varphi}_r^1$ gives

$$\gamma\tilde{\varphi}_r^1 + \frac{\partial\tilde{\varphi}_z^0}{\partial z} = 0. \quad (12c)$$

Taking the Hankel transform of order one of equation 11d and noting that

$\mathcal{H}_1\left(\frac{\partial\varphi_z}{\partial r}\right) = -\gamma\tilde{\varphi}_z^0$ gives

$$\left(\tilde{u}_\theta^1 - \zeta\frac{\partial\tilde{u}_\theta^1}{\partial z}\right)\bigg|_{z=0} = \left(\frac{\partial\tilde{\varphi}_r^1}{\partial z} + \gamma\tilde{\varphi}_z^0\right)\bigg|_{z=0}$$

$$= \dot{\theta}\frac{r^2}{\gamma}J_2(\gamma r) \quad (12d)$$

where $\tilde{u}_\theta^1 = \mathcal{H}_1(u_\theta(s))$.

The solution to equations 12a and b is given by

$$\tilde{\varphi}_r^1 = Ae^{kz} \text{ and } \tilde{\varphi}_z^0 = Be^{kz} \quad (13a,b)$$

where $k = \sqrt{\gamma^2 + \frac{s}{\nu_o}}$ and A and B are unknown constants. Substituting equations 13a, and b into equations 12c,d, solving for the unknowns constants and substituting back into equations 13a,b gives

$$\tilde{\varphi}_r^1 = \frac{\dot{\theta}}{s/\nu_o}\frac{k}{\gamma}\frac{e^{kz}}{(1+\zeta k)}r^2 J_2(\gamma r)\Big|_{r_i}^{r_o} \quad (14a)$$

$$\tilde{\varphi}_z^0 = -\frac{\dot{\theta}}{s/\nu_o}\frac{e^{kz}}{(1+\zeta k)}r^2 J_2(\gamma r)\Big|_{r_i}^{r_o}. \quad (14b)$$

In the γ (Hankel) domain, the shear stress on the top of the disk is given by

$$\mathcal{H}_1(\tau) = \tilde{\tau}^1 = \mu_o\frac{\partial \tilde{u}_\theta^1}{\partial z}. \quad (14c)$$

Substituting 14a and b into the Hankel transform of 11c and the result into 14c gives,

$$\tilde{\tau}^1 = \mu_o\dot{\theta}\frac{k}{\gamma(1+\zeta k)}r^2 J_2(\gamma r)\Big|_{r_i}^{r_o}. \quad (14d)$$

Taking the inverse Hankel transform of order one gives

$$\tau(r) = \mathcal{H}_1^{-1}(\tilde{\tau}^1) = \int_0^\infty \tilde{\tau}^1 J_1(\gamma r)\gamma d\gamma$$

$$= \mu_o\dot{\theta}\int_0^\infty \frac{k}{(1+\zeta k)}\left(r_o^2 J_2(\gamma r_o) - r_i^2 J_2(\gamma r_i)\right)J_1(\gamma r)d\gamma \quad (14e)$$

Notice that $J_2(\eta)$ goes to $\frac{1}{\sqrt{\eta}}$ as $\eta \to \infty$ and that $k \to \gamma$ for $\gamma \to \infty$, it can be shown that $\tilde{\tau}^1$ does not go to zero as $\gamma \to \infty$ for $\zeta = 0$. Therefore, the integrand of the integral in equation 14e is not bounded for all r without slip at the interface. Nevertheless, the torque T_{f_2} on the top of the disk can still be determined for any ζ. Noting that

$$T_{f_1} = 2\pi\int_{r_i}^{r_o} r^2 \tau dr, \quad (15a)$$

and substituting equation 14e into equation 15a, shifting the order of integration and simplifying gives

$$C_1 = \frac{T_{f_1}}{\dot{\theta}} = 2\pi\mu_o\int_0^\infty \frac{k}{\gamma(1+\zeta k)}\left(r^2 J_2(\gamma r)\Big|_{r_i}^{r_o}\right)^2 d\gamma \quad (15b)$$

Note that for all values of γ, the integrand in equation 15b is bounded. Thus, equation 15b can be evaluated numerically using Newton-Cotes integration formulas [15].

Equation 15b is a closed form solution for the loading on top of the disk. This loading takes on an interesting form. If we let $s = i\omega$, then the frequency response of this loading can be plotted. This is shown in Figure 4 for $g = 10.5\mu m$. For $0 \le \zeta \le 0.8$, the response of this plot varies little with ζ. Notice that at low frequencies the phase of this response is zero and the magnitude is a constant. Therefore, the transfer function between torque and rotation rate is a constant. Nevertheless, as the frequency is increased, the slope of the magnitude goes to $10 dB/decade$ and the phase goes to $45°$. This represents the response of the irrational transfer function,

$$\frac{T_{f_2}}{\dot{\theta}} = E\sqrt{s} \quad (16a)$$

where E is a constant. The value of E can be determined by returning to equation 15e and letting $\omega \to \infty$ and $\zeta = 0$. This equation becomes

$$\tau(r) = \mu_o\dot{\theta}\sqrt{\frac{s}{\nu_o}}\int_0^\infty\left(r_o^2 J_2(\gamma r_o) - r_i^2 J_2(\gamma r_i)\right)J_1(\gamma r)d\gamma$$

$$= \mathcal{H}_1^{-1}\left(\frac{1}{\gamma}\left(r_o^2 J_2(\gamma r_o) - r_i^2 J_2(\gamma r_i)\right)\right) \quad (16b)$$

However, noting that

$$\mathcal{H}_1(r\{H(r-r_o) - H(r-r_i)\})$$

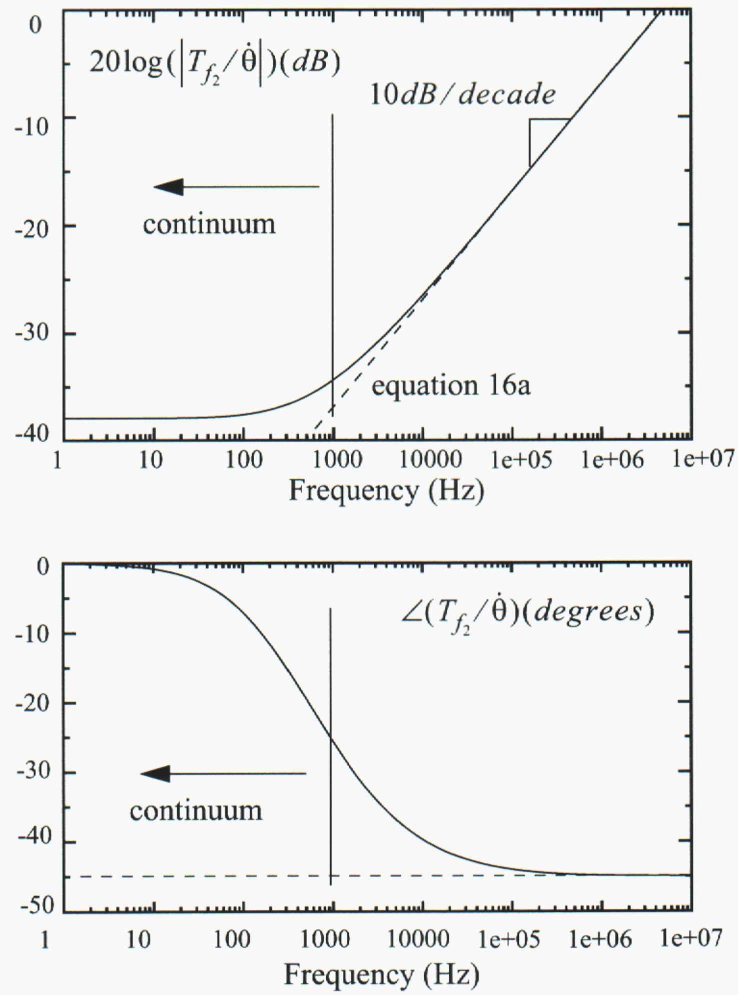

Figure 4: Frequency Response of $T_{f_1}/\dot{\theta}$, - equation 15b, -- high frequency approximation (equation 16a).

$$= \frac{1}{\gamma}(r_o^2 J_{2(\gamma r_o)} - r_i^2 J_{2(\gamma r_i)}) \quad (16c)$$

where $H(r)$ is a Heaviside function [10], equation 16b becomes

$$\tau(r) = \begin{cases} \mu_o \dot{\theta} r \sqrt{\dfrac{s}{\nu_o}} & \text{for} \quad r_i \le r \le r_o \\ 0 & \text{otherwise} \end{cases} \quad (16d)$$

Substituting 16d into 15a gives equation 16a where

$$E = \frac{\pi(r_o^4 - r_i^4)}{2}\sqrt{\rho_o \mu_o} \,. \quad (16e)$$

Equation 16a is also shown in Figure 4.

Fluid Loading on the Bottom of the Disk

If g is much smaller than the shear wavelength, then the velocity field varies almost linearly across the gap. Assuming a linear velocity distribution, the incremental force on the disk is given by

$$dT_{f_2} = 2\pi\mu_o\left(\frac{1}{1+\zeta/g}\right)\frac{r^3\dot{\theta}}{g}dr. \qquad (17a)$$

Integrating (17a) over the limits of the disk gives,

$$C_2 = \frac{T_{f_2}}{\dot{\theta}} = \frac{\pi\mu_o}{2g}\left(\frac{1}{1+\zeta/g}\right)(r_o^4 - r_i^4) \qquad (17b)$$

where T_{f_2} is the total torque on the disk due to the fluid within the gap.

If g is large, the wave solution must be solved for within the gap. This is performed by returning to equations 13a,b and including wave effects in the positive and negative axial z directions. These equations take the form

$$\tilde{\varphi}_r^1 = Ae^{kz} + Be^{-kz} \text{ and} \qquad (18a)$$

$$\tilde{\varphi}_z^0 = Ce^{kz} + De^{-kz}. \qquad (18b)$$

where $k = \sqrt{\gamma^2 + \frac{s}{\nu_o}}$ and A, B, C, and D are unknown constants. Using the boundary conditions

$$\left.\left(\hat{u} - \zeta\frac{\partial}{\partial z}(\hat{u}\cdot\hat{\theta})\right)\right|_{z=g} = \dot{\theta}r\hat{\theta}$$

$$\text{for } r_i \le r \le r_o \qquad (19a)$$

and

$$\left.\left(\hat{u} - \zeta\frac{\partial}{\partial z}(\hat{u}\cdot\hat{\theta})\right)\right|_{z=0} = 0$$

$$\text{for } r_i \le r \le r_o \qquad (19b)$$

gives

$$Ax = B \qquad (20a)$$

where

$$A = \begin{bmatrix} (k+\zeta k^2)e^{kg} & (-k+\zeta k^2)e^{-kg} & (\gamma+\zeta\gamma k)e^{kg} & (k+\zeta\gamma k)e^{-kg} \\ k-\zeta k^2 & -k-\zeta k^2 & \gamma-\zeta\gamma k & \gamma+\zeta\gamma k \\ \gamma e^{kg} & \gamma e^{-kg} & ke^{kg} & -ke^{-kg} \\ \gamma & \gamma & k & -k \end{bmatrix}$$

$x = \begin{bmatrix} A & B & C & D \end{bmatrix}^T$ and

$B = \begin{bmatrix} r^2 J_2(\gamma r) & 0 & 0 & 0 \end{bmatrix}^T$. Then,

$$C_2 = \frac{T_{f_2}}{\dot{\theta}} = 2\pi\int_0^\infty \frac{w(\gamma)}{\gamma} r^2 J_2(\gamma r)\Big|_{r_i}^{r_o} d\gamma \qquad (20b)$$

where

$w(\gamma) = \begin{bmatrix} k^2 & k^2 & \gamma k & -\gamma k \end{bmatrix} x$. Equations 20ab can be solved for using numerical matrix inversion and Newton-Cotes integration [15].

Free Response of the Disk in Fluid

The free response of the Figure 1 device can be found by forming a rational model, applying initial conditions, and simulating. Combining equations 6b, 7, 8b, and 15b gives

$$\frac{T}{\theta} = \frac{1}{Ms^2 + Cs + K} \qquad (21a)$$

where $C = C_1 + C_2$.

With the aid of an inverse Discrete Fourier Transform [16] and curve fitting techniques, the state space representation can be found as

$$\dot{\hat{x}} = \boldsymbol{A}\hat{x} + \boldsymbol{B}T \qquad (22a)$$

$$\theta = \boldsymbol{C}\hat{x}. \qquad (22b)$$

The free response of the disk for $g = 10.5\mu m$ is shown in Figure 5a. The resonate frequency was about 200Hz and the damping ratio was about 0.16. The free response of the disk for for $g = 2.0\mu m$,

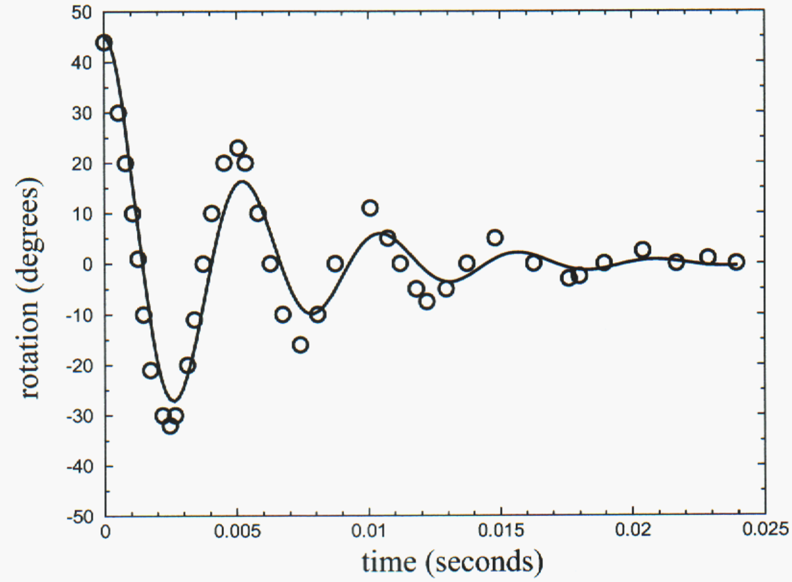

Figure 5a: Free Response of Resonator with 10um gap, o- experiment, -- theory.

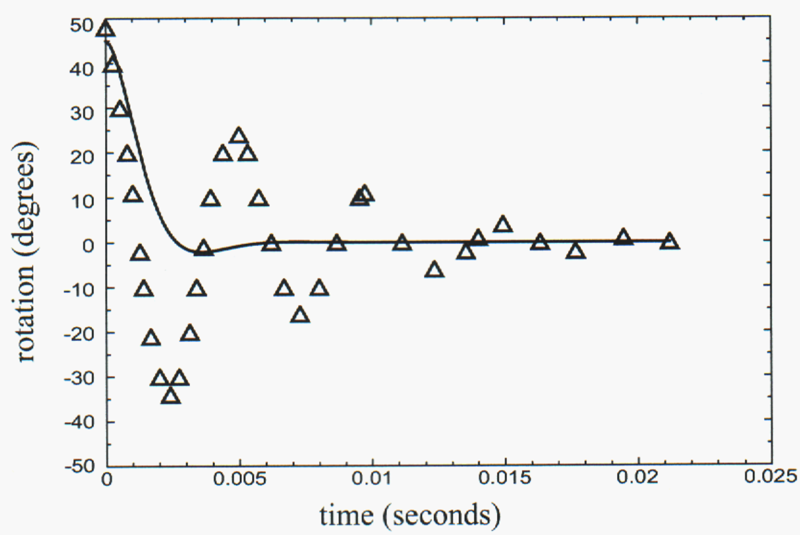

Figure 5b: Free Response of Resonator with 2um gap, Δ - experiment, -- theory.

shown in Figure 5b, had a damping ratio of 0.7.

Experimental Analysis

Experimental analysis was performed to validate the above damping model. Devices were manufactured using SUMMiT V™ technology [5] and testing was performed in air at room temperature and pressure.

By using a micro probe to move the disk to a desired angular location (i.e. 45°) and releasing the disk by lifting up on the probe, the free response of the disk could be measured on a high speed camera (see Figure 6).

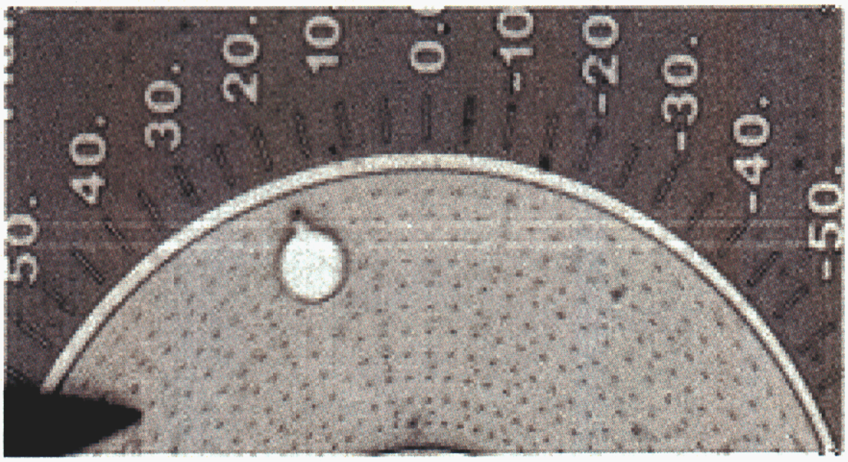

Figure 6: Light photo of resonator during free response, the probe (on left) is used to release the disk.

Experimental results are shown in Figure 5a and b. These results show that both the 10.5 and 2.0 μm devices had resonate frequencies around 200Hz, and surprisingly, both had damping ratios of about 0.1. The response of the device with a 10.5 μm gap and that with a 2.0 μm gap were almost the same.

To confirm that this was not an error in the measurement process or design, the poly layers of the two devices were rechecked, and the coating on the structure reexamined. The polylayers designs were confirmed to be correct and the structure was CO_2 dried. Therefore, no coatings existed on the surface that could alter damping. To confirm that residual stress was not producing variations in the gap, laser interferometry, SEM, and atomic force microscopy were used. As verified by laser interferometry, little variation in the static deflection of the structure occurred. Less than 0.5 μm of static deflection occurred in the 2 μm device and less than 1.0 μm of static deflection occurred in the 10.5 μm device. Moreover, using atomic force microscopy and a SEM, the gap between the top of the disk and the substrate was confirmed to be correct. As a further validation that the experiments were performed correctly, they were repeated for different devices on different modules. The results were the same.

Tests were also performed in vacuum and under pressure (see Figure 7a). The effect of a pressure change was to alter the mean free path of the air. In Figure 7b plots of these results are shown. An increase in pressure did little to alter the response of the disk. Nevertheless, as the pressure was dropped to a vacuum, the response became very lightly damped as expected.

Conclusions

As shown above, results did not match theory. From existing theory [8,9], the zero velocity condition at the wall should have been nearly valid. The Knudsen number (Kn) for the 2.0 μm device was 0.03 which places the fluid in the Newtonian region with small slip. The Knudsen number of the 10.5 μm device was 0.0057 which places the fluid in the zero slip

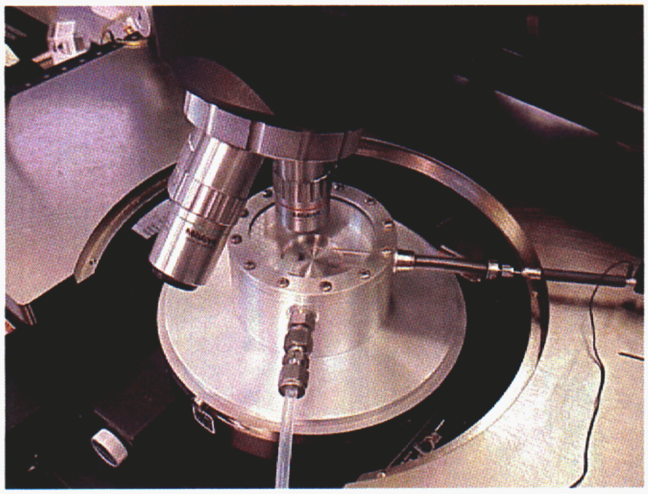

Figure 7a: Pressure and vacuum chamber used to vary MEMS environment

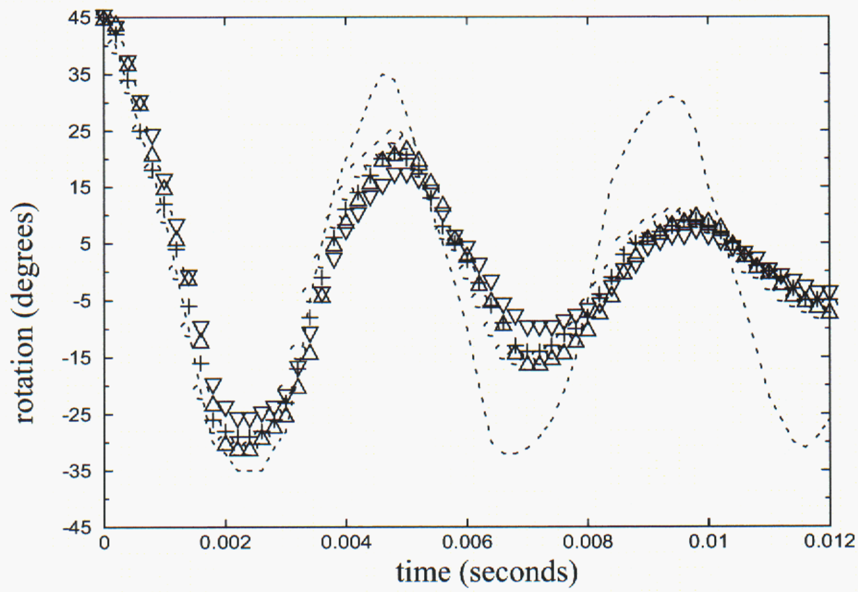

Figure 7b: Measured Response of Device inVarious Pressure Environments: - - at 120mTorr, o- at 0psig, Δ - at 15psig, + - at 30 psig, ∇ - at 45psig.

region. Therefore, existing theory states that the fluid should have been able to be treated as Newtonian with little slip at the walls. Nevertheless, the opposite was true.

If existing theory is wrong and a strong slip condition existed at the wall, these results could be better explained. The slip condition would dominate the force on the plate and therefore, the response would not be a function of the gap. As shown in Figure 8, two devices, similar in every respect except the gap, would have similar responses. The problem with this explanation is that the accommodation coefficient would have to be much smaller. As was stated earlier, this coefficient is usually between 0.2 and 0.8. Nevertheless, as shown in Figure 8, an accommodation coefficient of 0.01, comes close to mea-

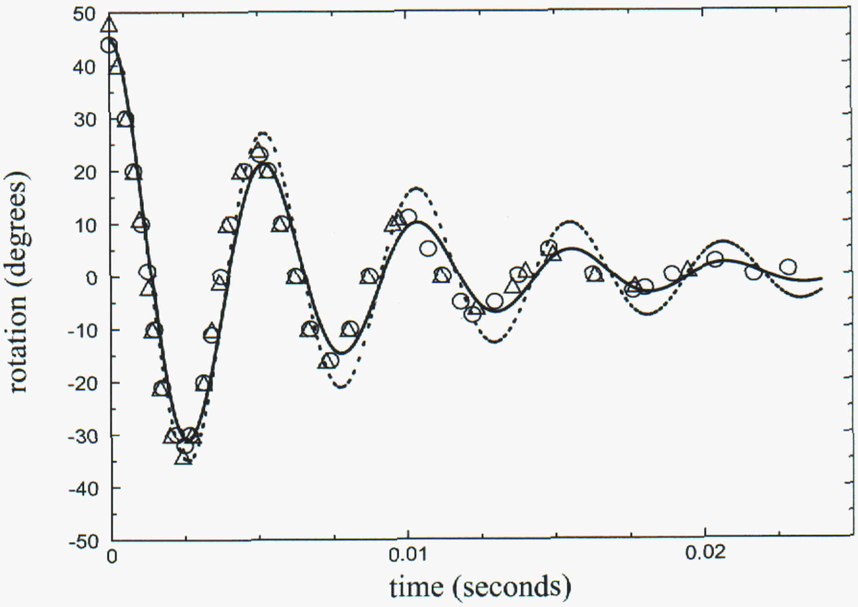

Figure 8: Measured and Theoretical Response of Device: o - experimental data for $g = 10.5\mu m$, Δ - experimental data for $g = 2.0\mu m$, . . - theory for $\sigma_v = 0.01$ and $g = 10.5\mu m$, - - theory for $\sigma_v = 0.01$ and $g = 2.0\mu m$.

sured data. An accomodation coefficient of this size would imply that little molecular energy is lost when an air molecule strikes the wall.

The present research points to the fact that existing theory for air damping in micro devices is incomplete. Further research is needed to better understand what is happening at the surface of these devices. This could have significant impact in reducing the losses in MEMS.

References

1. Y.-H. Cho, B.M. Kwak, A.P. Pisano and R.T. Howe 1993 *Proc. IEEE Micro Electro Mechanical Systems Workshop (MEMS'93), Fort Lauderdale, FL, USA, Feb. 7-10,* 93-98. Viscous energy dissipation in laterally oscillating planar microstructures.
2. Y.-H. Cho, B.M. Kwak, A.P. Pisano and R.T. Howe 1994 *Sensors and Actuators A*, **40**, 31-39. Slide film damping in laterally driven microstructures.
3. S.W. Wenzel 1982 *Ph.D Thesis, Department of Electrical engineering and Computer Sciences, University of California, Berkeley, CA*. Applications of ultrasonic lamb waves.
4. J.L. Dohner 1998 *Journal of Sound and Vibration*, **217**(1), 113-126. The contribution of radiation and viscous loss in a fluid loaded flexural plate wave sensor.
5. E.R. Shepherd *Sandia Report SAND2002-2773C, Sandia National Laboratories, Albuquerque, NM.* Prototyping with SUMMiT technology, Sandia's Ultra-planar multi-level MEMS technology.

6. The original concept for this device was developed by Kelly Klody, Electromechanical Engineering, Sandia National Laboratories.

7. F.P. Beer and E.R. Johnston, Jr. 1981 *Mechanics of Materials.* McGraw-Hill Book Company, New York.

8. J.R. Torczynski, M.A. Gallis, E.S. Piekos, 2002, *Modeling and Simulation of Gas Forces on Moving Microstructures*, Sandia Internal Memorandum.

9. D. Jie, X. Diao, K.B. Cheong, and L.K. Yong, *Journal of Micromechanics and Microengineering*, **10**, 372-379, Navier-Stokes simulations of gas flow in micro devices.

10. F.B. Hildebrand 1976 *Advanced Calculus for Applications*. Prentice-Hall, Inc., Englewood Cliffs, NJ.

11. S.Temkin 1981 *Elements of Acoustics*. John Wiley & Sons, New York.

12. J.D. Achenbach 1984 *Wave Propagation in Elastic Solids*. North-Holland, New York.

13. I.N. Sneddon 1972 T*he Use of Integral Transforms*. McGraw-Hill Book Company, New York.

14. M.C. Junger and D. Feit 1986 *Sound, Structures, and Their Interaction, Second Edition*. The MIT Press, Cambridge MA.

15. C.F. Gerald 1980 *Applied Numerical Analysis, Second Edition*. Addison-Wesley Publishing Company, Reading, MA.

16. A.B. Oppenheim and R.W. Schafer 1975 *Digital Signal Processing*. Prentice-Hall Inc. Englewood Cliffs, NJ.

Appendix: A:

Table 1: Parameter values

Parameter	r_o	r_i	r_h	t	g	w
Numerical value and dimensions	$400\mu m$	$160\mu m$	$30\mu m$	$2.25\mu m$	$10.5\mu m$ $2.0\mu m$	$2.5\mu m$

Parameter	ρ_o	μ_o	E	ρ
Numerical value and dimensions	1.197×10^{-18} $(kg/\mu m^3)$	18×10^{-12} $(\mu N\cdot s/\mu m^2)$	160000 $(\mu N/\mu m^2)$	2.32×10^{-15} $(kg/\mu m^3)$

The above data can be obtained from the following references:

W.N. Sharpe Jr., B. Yuan and R. Vaidyanathan 1997 *Proceedings of IEEE, The Tenth Annual International Workshop on Micro Electro Mechanical Systems, An Investigation of Micro Structures Sensors, Actuators, Machines and Robots, MES97* 424-429. Measurements of Young's modulus, Poisson's ratio, and tensile strength of polysilicon.

R.E. Bolz and G.L. Tuve 1981 *CRC Handbook of tables for Applied Engineering Science, 2nd Edition.* CRC Press, Inc. Boca Raton, Florida.

Intentionally Left Blank

Distribution List

MS1080 1769 J.Dohner (10)
MS1080 1769 J. Allen
MS1080 1769 D. Carr
MS1080 1769 D. Dagel
MS1310 1769 M. Baker
MS1080 1769 P. Galombos
MS1080 1769 B. Huber
MS1080 1769 J. Conrad
MS1080 1769 M. Jenkins (3)
MS1080 1769 D. Sandison

MS1310 1762 M. De Boer
MS1310 1762 F. Sexton
MS1310 1762 D. Tanner

MS1080 1749 H. Stewart
MS1080 1749 J. Fleming
MS1080 1749 M. Okandan

MS0889 1851 M. Dugger

MS1310 2614 M. Duesterhaus
MS1310 2614 R. Kellogg
MS1310 2614 K. Klody
MS1310 2614 M. Polosky
MS1310 2614 G. Sleefe

MS0826 9113 J. Torczynski
MS1310 9113 C. Wong
MS0827 9113 M. Gallis
MS0826 9113 S. Kempka

MS0847 9124 F. Bitsie
MS1310 9124 B. Ozdoganlaro
MS0847 9124 J. Redmond
MS0847 9124 H. Sumali

MS0847 9127 C. Fulcher

MS0835 9142 T. Walsh
MS0835 9142 K. Alvin

R. Howe
Ept. of EECS
231 Cory Hall
Berkeley CA 94720-1770 USA

H. Stafford
University of Oklahoma
Aerospace & Mechanical Eng.
100 East Boyd, Room 510
Norman, Okalahoma 73019-1006

MS9018 8945-1 Central Tech. Files
MS0899 9616 Tech. Library (2)